This is a Just Accepted version, keep updated with https://doi.org/10.26599/OCEAN.2026.9470034
OCEAN 2026, 2, 9470034

Research Article

https://doi.org/10.26599/OCEAN.2026.9470034

An invisible bioelectric barrier: Electric-eel-inspired low-power underwater defense method

Shuai Wu, Chenxu Wang, Xiao He, Changhua Li and Chunwei Cai*

School of New Energy, Harbin Institute of Technology, Weihai 264209, China

Address correspondence to Chunwei Cai, caichunwei@hit.edu.cn
Received: June 30, 2026 / Revised: September 23, 2026 / Accepted: November 5, 2026

ABSTRACT

Physical underwater barriers can obstruct navigation and aquaculture operations and often require substantial fixed infrastructure. This study presents an electric-eel-inspired bioelectric barrier prototype that produces controllable pulsed electric fields from a low-voltage supply. The biomimetic contribution has two components: reproduction of the measured high-voltage electric-organ-discharge (EOD) timing (100 Hz repetition and 2.5 ms active width), and a six-stage Marx cascade that provides an engineering analogue of serial electrocyte voltage summation. With a 5–10 V DC input, the prototype generated stable pulses across 28–500 Ω resistive loads and reached 53 V, corresponding to a peak voltage-transfer ratio of 88% relative to the ideal sixfold sum. The measured time-averaged load power ranged from 0.3 to 14.5 W. Prototype experiments show clear amplitude-dependent behavioral responses in fish and stronger responses to EOD-like pulses than to DC stimulation under the tested conditions. These results demonstrate the circuit-level feasibility of a low-power, contactless bioelectric barrier and provide a technical basis for bioinspired underwater defense.

KEYWORDS: bioelectric barrier; electric eel; electrocyte cascade; low-power pulsed power supply; underwater defense; bioinspired engineering

1 Introduction

Ports, water intakes, aquaculture facilities, and critical underwater infrastructure require deterrent systems that do not permanently obstruct navigation or water exchange [1]. A bioelectric barrier offers one possible non-physical approach: electrodes establish a localized electric field only when a monitored target enters a protected zone, as shown in Fig. 1. The engineering objective is therefore not indiscriminate electrification of a water body, but time-limited and spatially constrained pulse delivery under monitored operating conditions.

Just Accepted

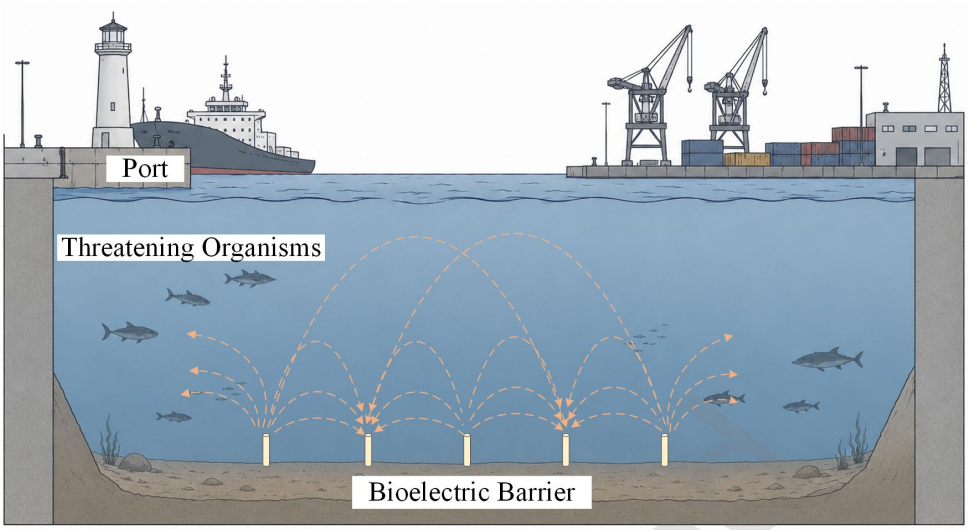


Figure 1 Conceptual scenario of the proposed bioelectric barrier.

The value of bioinspired marine engineering lies not in copying biological appearance, but in translating biological mechanisms into engineering principles [2]. For an underwater bioelectric barrier, the central challenge is not voltage boosting alone. The source must generate biologically relevant pulses from a low-voltage supply, preserve pulse fidelity under conductive loading, and recover energy rapidly between adjacent discharge periods to sustain repeated operation.

The electric organ of *Electrophorus electricus* provides a biological reference for this problem. Electric eels vary electric-organ discharge (EOD) patterns with behavioral context: weak discharges support electrolocation, whereas strong trains are used during predation and defense [3–6]. At the cellular level, neural activation synchronizes thousands of polarized electrocytes; the transcellular potentials add along serial stacks, while parallel stacks increase available current [7–9,23–26]. Recent work on model electrocytes further emphasizes that rapid synchronization, as well as series voltage addition, is central to the biological discharge mechanism [23].

Electrical barriers and guidance systems are not new. Reviews and field studies show that pulsed or low-voltage electric fields can deter or redirect fish, but performance depends on species, body length, pulse waveform, water conductivity, flow velocity, and electrode geometry [16–22]. For example, the NEPTUN system used a continuously energized 50–80 V inhomogeneous field [17], whereas hybrid FishProtector systems combined a physical rack with a low-voltage electric cue [18]. Recent controlled studies have quantified size-dependent passage, injury risk, behavioral thresholds, and frequency–flow interactions [19–22]. These studies establish the application context, but none adopts a bioinspired source architecture. To

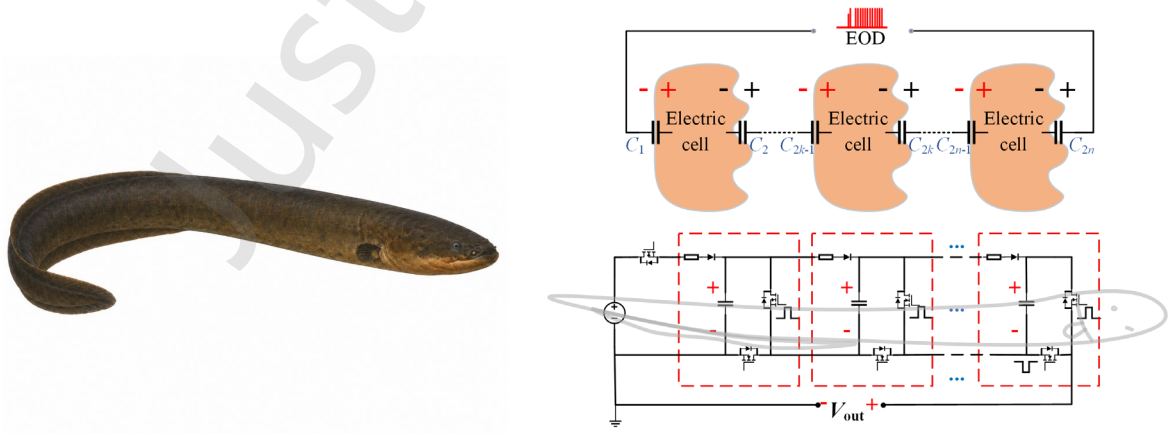
Just Accepted

the best of our knowledge, no bioinspired electric barrier based on an electrocyte-mapped low-voltage source has been reported, and the present electric-eel-inspired, low-power underwater defense method aims to address this gap.

Against this background, the contribution is concentrated in two biomimetic translations. First, the programmable Marx source reproduces the temporal signature extracted from measured high-voltage electric-eel EODs, namely a 100 Hz train with a 2.5 ms active interval. Second, the six-stage cascade provides a structural analogue of the serial electrocyte organization: each low-voltage stage stores charge independently and contributes one voltage increment during synchronized series discharge. Conventional Marx generators are mainly designed for kilovolt-class pulsed-power systems or for loads unlike conductive underwater media [10–15]. The novelty is therefore not the Marx principle itself, but the joint waveform-level and architecture-level translation of the eel mechanism into a low-voltage, high-repetition source for conductive water loads.

The prototype developed here realizes a two-level biomimetic mapping from a 5–10 V low-voltage supply to EOD-like pulsed output. We systematically evaluate pulse fidelity, load adaptability, voltage efficiency, input power, and output efficiency. A water-tank platform is then used for exploratory biological tests to compare the behavioral stimulation produced by the generated EOD-like waveform and by DC exposure, providing experimental evidence for the potential use of biomimetic bioelectric barriers in underwater defense.

2 Electric Eel Discharge Fundamentals and Biomimetic Inspiration



(a) (b)

Figure 2 Biological foundation and biomimetic design strategy. (a) Electric eel. (b) Biomimetic translation from electrocyte voltage summation to cascaded circuit discharge.

The electric eel is often described as a biological generator. Its remarkable discharge capability arises from a specialized electric organ, as shown in Fig. 2a. This organ contains numerous

electrocytes that discharge synchronously under neural control, producing high-frequency, high-voltage EOD waveforms. Inspired by both the neural timing of high-voltage EODs and the biological mechanism of cellular series connection and potential summation, we propose a biomimetic design strategy in which discrete energy-storage units emulate electrocytes and a dedicated circuit topology enables cascaded discharge for voltage summation and pulsed output, as shown in Fig. 2b.

2.1 EOD Behaviors and Waveform Targets

Electric eels generate three representative classes of EOD waveforms, as shown in Fig. 3: high-frequency high-voltage pulses, doublet or triplet pulses, and low-voltage probing pulses. These waveform classes correspond to distinct behavioral modes. During predatory attacks, electric eels mainly employ direct strikes and coiling attacks, both of which are accompanied by dense high-frequency, high-voltage discharge trains; therefore, this study focuses on this waveform class. Doublet or triplet EODs are primarily associated with defensive behaviors and can function as warning, deterrent, or expulsion signals. During routine activities, electric eels use low-frequency, low-voltage pulses to detect surrounding conductive objects and locate potential targets.

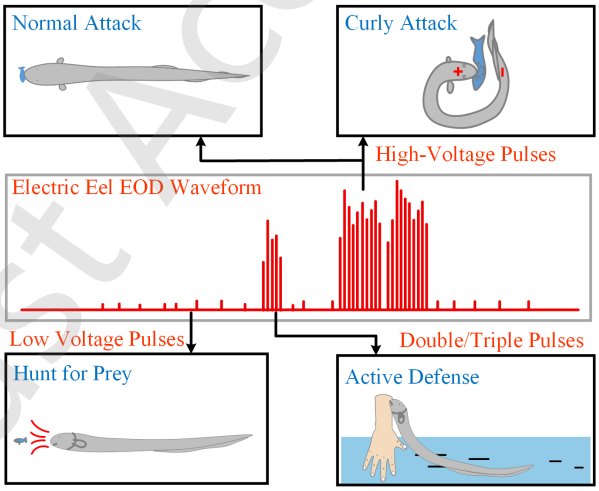


Figure 3 Functional classification of electric eel EOD behaviors and waveform patterns.

The 100 Hz repetition rate and 2.5 ms active interval were selected primarily for biological fidelity. They were extracted from the measured high-voltage EOD waveform used in the underlying design study and fall within the reported strong-EOD regime of electric eels [3–6]. Accordingly, these parameters are not claimed to be universally optimal for deterrence, but they are the reference waveform that the present biomimetic circuit was required to reproduce. Firmware permits other frequencies and widths, enabling a later sensitivity study without changing the main topology.

Just Accepted

2.2 Electrocyte Architecture and Voltage-Summation Mechanism

From an electrical-modeling perspective, the core mechanism of parallel charging and series discharge in electric eel electrocytes can be represented by a capacitive network, as shown in Fig. 4. The membrane of a single electrocyte is modeled as a capacitive unit. The posterior membrane corresponds to an odd-numbered capacitor C_{2k-1} (k = 1, 2, ...), whereas the anterior membrane corresponds to an even-numbered capacitor C_{2k} (k = 1, 2, ...). In the resting state, the negative terminals of the capacitors share the intracellular node and the positive terminals share the extracellular node, forming a parallel topology. When an action potential triggers discharge, the polarity of the odd-numbered capacitors reverses and the capacitive units are reconfigured into a series loop. This electrical model captures the electrical essence of efficient electric eel discharge: topological reconfiguration of cell-level capacitive structures converts low-voltage energy storage into high-voltage output.

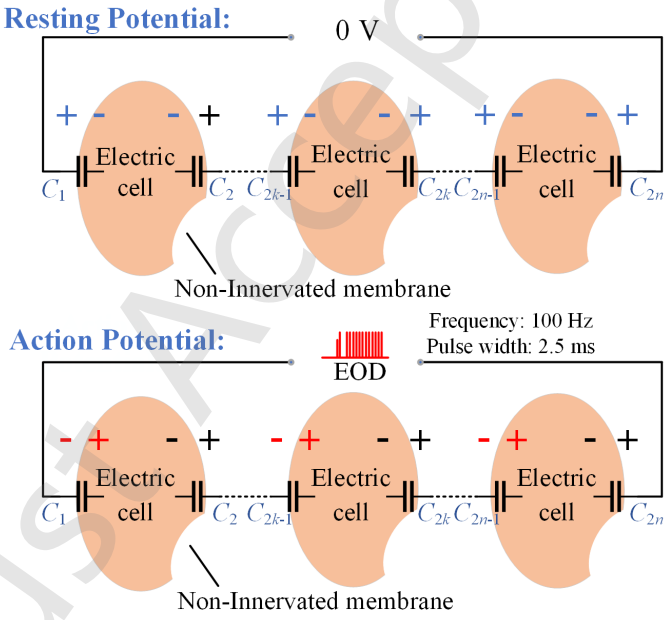


Figure 4 Schematic representation of electric eel electrocyte discharge.

3 Structure and Parameter Design of the Bioelectric Barrier Prototype

3.1 Design of the Main Circuit Topology for the Bioelectric Barrier

The operating principle of a Marx pulse generator matches the electric eel discharge mechanism in both structural analogy and functional outcome, making it a suitable basis for the bioelectric-barrier main circuit. The high-voltage discharge of the electric eel arises from the asymmetric membrane structure of electrocytes: under neural control, changes in membrane potential implement a physiological process equivalent to parallel charging

Just Accepted

followed by series discharge. In the corresponding Marx circuit, power-electronic switches connect the stage capacitors in parallel to a low-voltage DC source during charging. During discharge, the switching network reconfigures the circuit so that adjacent capacitors are connected in series, completing voltage summation and producing a high-voltage pulse.

For an n-stage Marx generator, the ideal output voltage is nV_{in}, where V_{in} is the DC input voltage and n is the number of cascaded stages. Because each charging diode introduces a forward voltage drop, the actual peak output voltage is lower than this ideal value. If only the diode drop is considered, the predicted peak is given by Eq. (1):

$$U_{out} = nV_{in} - \frac{n(n+1)}{2}\Delta U_D \tag{1}$$

In Eq. (1), U_{out} is the predicted peak output voltage considering only the charging-diode drop, and ΔU_D is the forward voltage drop of a single charging diode. The term $n(n+1)/2$ is the total number of diode drops along the charging path, because the i-th capacitor is charged through approximately i diodes, giving $1+2+\cdots+n=n(n+1)/2$.

A more complete non-ideal model is obtained by including the current-dependent discharge-path losses. The output peak is then approximated by

$$V_{out,pk} \approx U_{out} - I_{pk}[nR_{ESR} + N_{sw}R_{DS(on)} + R_{path}] \tag{2}$$

where $V_{out,pk}$ is the actual peak output voltage, I_{pk} is the peak load current, R_{ESR} is the equivalent series resistance (ESR) per stage capacitor, N_{sw} is the number of series MOSFETs in the discharge path, $R_{DS(on)}$ is the on-state resistance per MOSFET, and R_{path} is the interconnect and contact resistance.

To better emulate the electric eel EOD waveform at the functional level, the generator was designed for an output pulse frequency of f = 100 Hz, a pulse width of D = 2.5 ms, and a peak voltage of at least 50 V. In practical circuits, capacitor equivalent series resistance, switch conduction loss, and load discharge further reduce the pulse amplitude over time. Increasing stage count alone would raise device count, cumulative charging-path diode loss, switching complexity, and the energy that must be restored between pulses. The selected six-stage architecture instead balances voltage gain, recharge time, load tolerance, and control complexity.

Considering these requirements, the final main circuit of the bioelectric barrier is shown in Fig. 5. Each dashed module represents one energy-storage capacitor stage and is functionally analogous to an electric eel electrocyte. Each module contains a charging resistor R_{Ci}, a charging diode D_i, an energy-storage capacitor C_i, and two MOSFET switches, T_{Ci} and T_{Pi}.

Just Accepted

Isolated voltage and current sensing circuits were reserved in the hardware for future closed-loop regulation. Switching between the charging and discharge states realizes parallel charging and series discharge, forming a biomimetic circuit structure corresponding to the series arrangement of electrocytes.

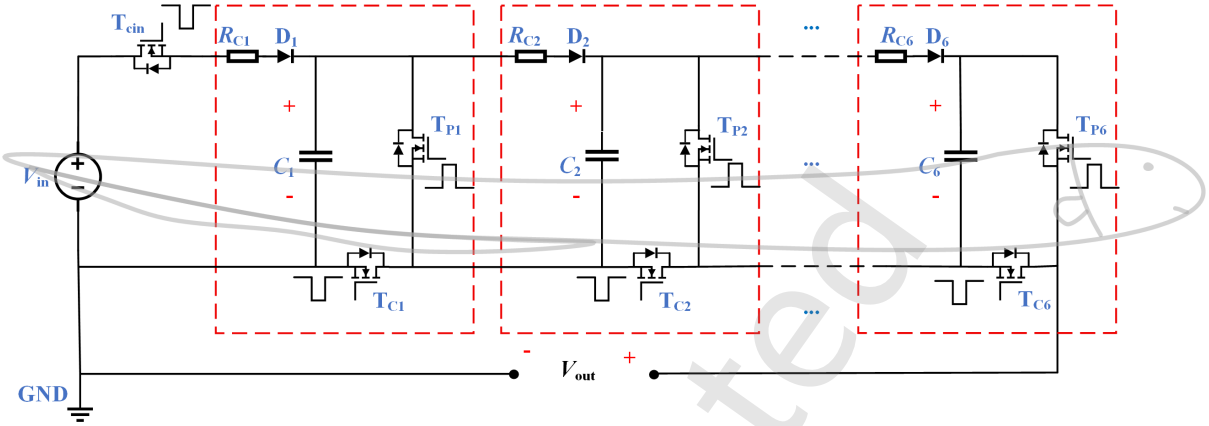


Figure 5 Main circuit of the bioelectric-barrier prototype.

3.2 Charge–discharge constraints and component selection

The timing relationship between capacitor charge–discharge behavior and pulse output is shown in Fig. 6. One complete operating period T contains two phases: a series-discharge interval from t_0 to t_1 and a parallel-recharge interval from t_1 to t_2. To keep the output pulse stable within the prescribed pulse width, each stage capacitor must retain a nonzero transition voltage U_{CV} at t_1 = 2.5 ms; otherwise, the output voltage decays rapidly before the pulse ends. To support repeated discharge in the next cycle, the stage voltages should recover close to the DC input voltage at t_2 = 10 ms. These requirements lead to two constraints: pulse retention during discharge and voltage recovery during recharge.

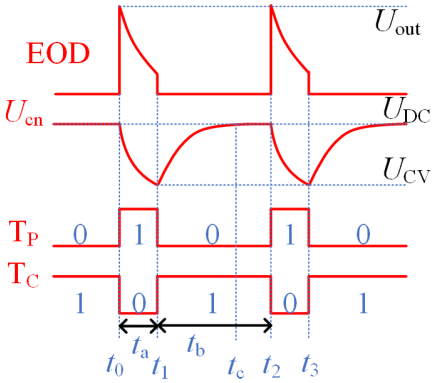


Figure 6 Pulse timing and capacitor charge–discharge waveform.

According to the average pulse width of the electric eel EOD waveform, $t_1 = DT = 2.5$ ms. A capacitor is generally considered practically discharged after five time constants. To ensure

Just Accepted

that residual voltage remains at t_1, that is, that the switching voltage U_{CV} remains greater than zero, the series-discharge process must satisfy $5\tau_1 \geq t_1 = DT = 2.5$ ms. This condition corresponds to the active-state constraint during series discharge.

After the circuit switches from the discharge state to the charging state, the stage capacitors must recover close to the DC input voltage within the remaining period. The required charging time t_c should therefore satisfy $t_c \leq t_2 - t_1 = (1 - D)T = 7.5$ ms. This condition corresponds to the resting-state constraint during parallel charging.

During series discharge, the equivalent capacitance of n capacitors in series is $C_S = C/n$, and the discharge time constant is $\tau_1 = R_L C_S$, where R_L is the load resistance. Because the capacitor voltage decays to approximately 0.67% of its initial value after five time constants, the 2.5 ms effective pulse width must occur before this practical discharge limit. This requirement yields the lower-bound capacitance constraint in Eq. (3).

$$t_1 = \tau_1 \ln \frac{U_{DC}}{U_{CV}} \tag{3}$$

During parallel recharge, the equivalent capacitance of n capacitors in parallel is $C_P = nC$, and the charging time constant is $\tau_2 = R_C C_P$, where R_C is the equivalent charging resistance used in the analytical model. The time required for the capacitor voltage to recover from the transition voltage U_{CV} to the DC input voltage U_{DC} is expressed by Eq. (4). Because capacitor voltage approaches U_{DC} asymptotically, practical full charge must be judged using an allowable voltage error.

$$t_c = \tau_2 [5 - \ln(\frac{U_{DC}}{U_{DC} - U_{CV}})] \tag{4}$$

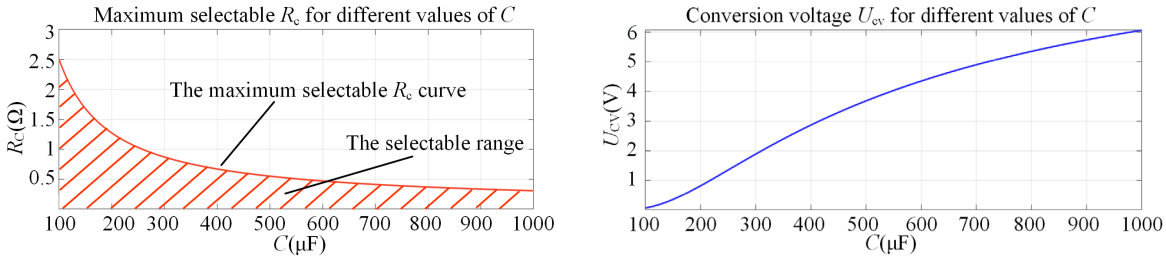
Combining the discharge-retention and recharge-recovery constraints with $C_S = C/n$ and $C_P = nC$ defines the feasible capacitance–resistance domain for EOD-like pulse generation. Substituting $n = 6$, $R_L = 30\ \Omega$, $T = 10$ ms, and $t_1 = 2.5$ ms gives $C \geq 100\ \mu$F. The corresponding upper bound on the equivalent charging resistance is given by Eq. (5).

$$R_C \leq \frac{1.25 \times 10^{-3}}{C[5 - \ln(\frac{1}{1 - e^{-\frac{5 \times 10^{-4}}{C}}})]} \tag{5}$$

Solving Eq. (5) gives the maximum selectable charging resistance R_C and the corresponding transition voltage U_{CV} for different capacitance values, as shown in Figs. 7a and 7b. The region enclosed by the maximum R_C curve and the coordinate axes represents the feasible parameter range satisfying both discharge-retention and recharge-recovery constraints. Based on this theoretical analysis and parameter optimization, the final hardware parameters of the main

Just Accepted

circuit were selected as listed in Table 1, including charging resistance R_{Ci}, switching frequency f, switching duty ratio D_S, and diode forward voltage V_f.



(a) (b)

Figure 7 Parameter-selection curves. (a) Allowable charging resistance as a function of stage capacitance for R_L = 30 Ω. (b) Predicted capacitor transition voltage UCV for R_L = 30 Ω.

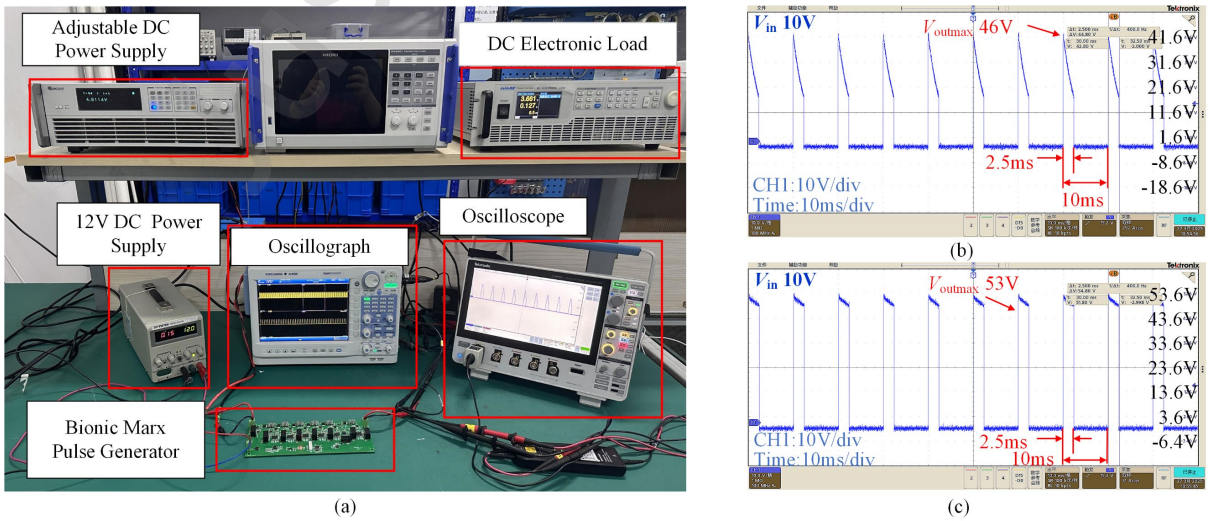
Table 1 Principal parameters of the bioelectric barrier prototype

Parameters	Values	Parameters	Values
V_{in}	0-10 V	f	100 Hz
C_i	440 μF	D_s	0.25
R_{Ci}	50 mΩ	V_f	0.35 V

4 Air Discharge and Underwater Biological Tests

4.1 Air discharge performance test

Before the underwater observations, the prototype was characterized with a programmable DC source, electronic loads, and voltage recording, as shown in Fig. 8a. Resistive loads from 28 to 500 Ω and inputs from 5 to 10 V were tested. At 10 V input, the measured peak increased from 46 V at 28 Ω to 53 V at 500 Ω; representative pulses are shown in Figs. 8b and 8c. The 100 Hz repetition rate and approximately 2.5 ms active interval were retained across the tested range.



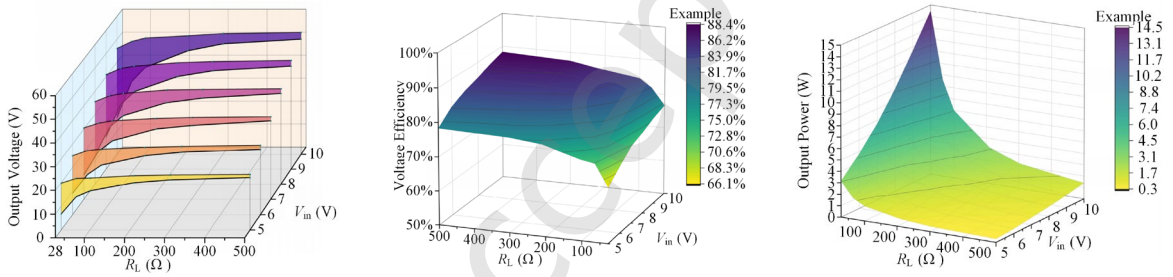
(a) (b) (c)

Figure 8 Electrical characterization setup and representative output waveforms. (a) Test arrangement. (b) Output waveform at the minimum tested load. (c) Output waveform at the maximum tested load.

Just Accepted

Figure 9 summarizes output voltage, voltage efficiency, and output power of the pulse generator for different input voltages and loads. These results characterize the output behavior and energy-conversion trend of the prototype across operating points and provide a basis for selecting parameters in subsequent underwater tests.

As shown in Fig. 9a, increasing load resistance reduces pulse droop and changes the output from a decaying trapezoid toward an approximately rectangular waveform. The voltage efficiency consequently rises with load resistance (Fig. 9b). At the maximum-power operating point (V_{in} = 10 V, R_L = 28 Ω), the recorded average input current was approximately 1.45 A, giving Pin ≈ 14.5 W and an input energy of 145 mJ per 10 ms period (Fig. 9c). The output waveform decreased from approximately 46 V to 17 V over the 2.5 ms active interval. Fitting this decay with a first-order exponential gives τ = 2.51 ms and E_{out} = 81.9 mJ per pulse, so the resulting waveform-based energy-efficiency estimate is therefore 56.5%.



(a) (b) (c)

Figure 9 Load-dependent electrical performance. (a) Output-voltage contour map under different input voltages and output loads. (b) Voltage-efficiency contour map under different input voltages and output loads. (c) Power contour map under different input voltages and output loads.

The measured results verify the design-stage prediction in Section 3.1. At V_{in}=10 V, the measured peak is 53 V at R_L=500 Ω and 46 V at R_L=28 Ω. These values can be interpreted using Eqs. (1) and (2). With n=6 and ΔU_D in the range 0.3–0.35 V, Eq. (1) predicts a diode-drop-limited peak between 52.65 V and 53.7 V.

At R_L=500 Ω, I_{pk}=0.11 A, so the current-dependent term in Eq. (2) is negligible, and the measured 53 V falls within the predicted 52.65–53.7 V interval. At R_L=28 Ω, however, I_{pk} rises to approximately 1.64 A, making the current-dependent term significant, so the measured peak decreases to 46 V, consistent with Eq. (2). The measured results therefore confirm that the cumulative charging-diode drop is the dominant loss term, while the residual difference is attributed mainly to capacitor ESR, interconnect resistance, and current-dependent diode behavior. Reducing the charging-diode drop remains the most effective single improvement, while changing stage count is better reserved for lower-impedance seawater operation.

Just Accepted

4.2 Exploratory Underwater biological discharge tests

Exploratory observations were conducted in a 100 cm × 50 cm × 40 cm freshwater tank with two opposing plate electrodes separated by approximately 1 m (Fig. 10a). The fish were purchased from a local retail market and acclimated for 24 h in the same laboratory water environment used for testing.

The EOD-like observations involved one mirror carp (1.8 kg), one common carp (1.3 kg), and one crucian carp (0.4 kg). The measured terminal resistance of the electrode–water arrangement was approximately 500 Ω, and the reference freshwater condition was set to 20 °C, σ = 0.04 S/m, and pH = 7. A programmable DC source supplied 2–10 V input voltage, and behavioral responses were observed and recorded at different output amplitudes. Representative observations are shown in Figs. 10b–10e, and the response comparison is summarized in Fig. 10f.

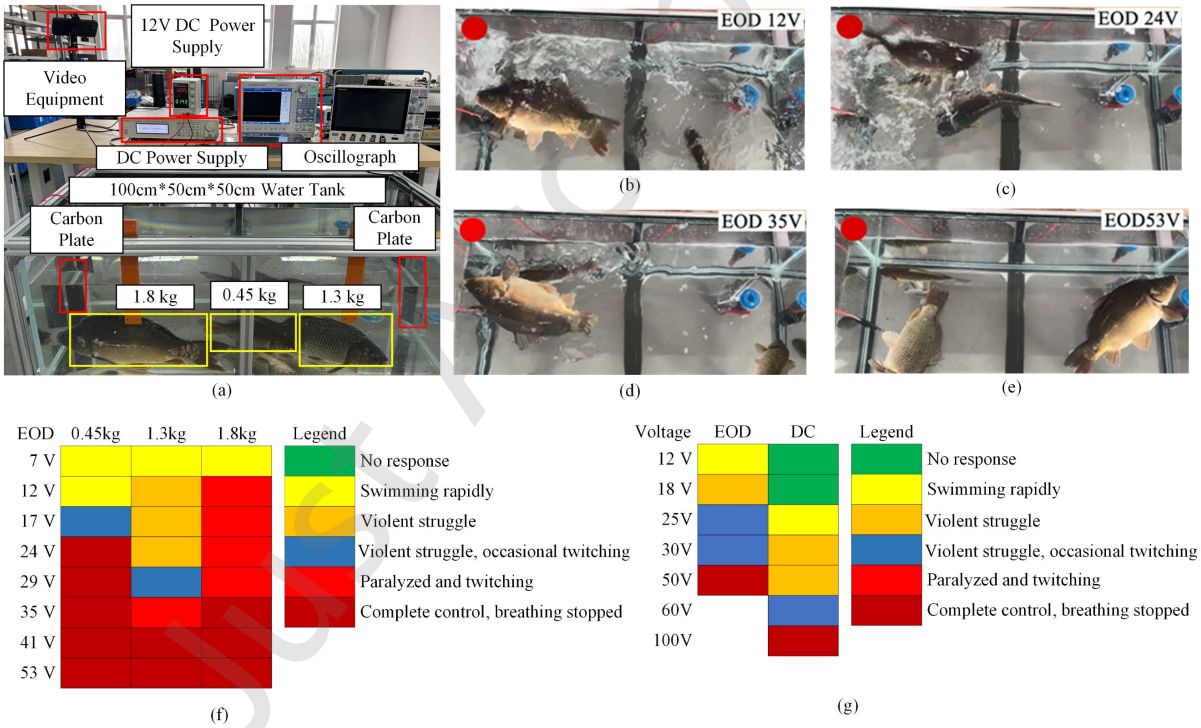


Figure 10 Exploratory underwater biological observations. (a) Water-tank and electrode arrangement. (b–e) Recorded responses at different pulse amplitudes. (f) Ordinal swimming-velocity and tail-beat comparison for the three fish tested (g) Near-amplitude comparison between EOD-like pulses and DC exposure.

Table 2 presents the behavioral results using two predefined ordinal indices, providing a more intuitive comparison across species and voltage levels. The swimming-velocity index (SVI) ranged from 0 (motion inhibition) to 3 (vigorous or disordered swimming), while the tail-beat index (TBI) ranged from 0 (no visible beating) to 3 (rapid or convulsive beating). The experimental results indicate that the bioelectric effect depends jointly on voltage level, fish

species, and body mass, with stronger immobilization observed at higher voltages, for larger body mass, and in species with greater sensitivity to the electric field. At 53 V peak, all tested fish showed marked motion inhibition, indicating that the generated EOD-like pulses can induce clear behavioral responses in an underwater environment.

Table 2 Quantitative response matrix based on ordinal swimming-velocity and tail-beat indices.

Species	Body mass	SVI/TBI (12 V)	SVI/TBI (24 V)	SVI/TBI (35 V)	SVI/TBI (53 V)
Mirror carp	1.8 kg	1/2	1/1	0/0	0/0
Common carp	1.3 kg	3/2	2/2	0/1	0/0
Crucian carp	0.4 kg	3/3	0/0	0/0	0/0

To further evaluate the role of EOD waveforms in biological stimulation, comparative tests were performed using EOD-like pulses and DC stimulation at similar peak voltages, as shown in Fig. 10g. Under the tested conditions, a near-amplitude exploratory comparison in a grass carp (1.2 kg) showed that EOD-like pulses induced stronger behavioral responses than DC stimulation at comparable peak voltages. These observations support the potential of biomimetic EOD waveforms for underwater deterrence and behavioral modulation, while broader efficacy and safety thresholds require dedicated dose-matched and replicated studies.

4.3 Electric-Field Distribution, Effective Range, and Controllability

At 100 Hz, water can be treated as a conductive medium in the quasi-static limit. For two approximately parallel plates, the average field is $E=V_{pk}/d$. With d=1 m, the measured 12–53 V pulses correspond to approximately 12–53 V/m across most of the inter-electrode region, which exceeds the 6.0–9.8 V/m response range reported for a different marine-fish waveform [21]. The main laboratory action zone is therefore approximately the 1 m inter-electrode region (1 m long, 0.5 m wide and 0.4 m deep). The field becomes nonuniform near and beyond the plate edges, and species sensitivity differs, so the present data do not define a precise external deterrence boundary. However, for larger protected zones, multiple electrode modules can be arranged in an array with overlapping action zones to extend the effective barrier range beyond a single electrode pair.

According to Laplace's equation, conductivity does not alter the normalized field shape or the programmed 100 Hz / 2.5 ms timing in homogeneous water. Higher seawater conductivity, however, lowers the load resistance and increases source current. For a current-limited generator, this causes greater amplitude droop and reduces the effective range. The prototype preserved timing over 28–500 Ω, and the circuit simulation retained the waveform at 15 Ω, but with increased droop. Seawater is therefore expected mainly to reduce pulse amplitude, while

Just Accepted

leaving frequency and pulse width unchanged within the source's current capability. Turbidity is not expected to significantly affect the low-frequency field, and ground returns from nearby structures or the seabed require geometry-matched analysis.

The design objective is to trigger a neural and neuromuscular response, not to deliver energy in proportion to body mass. For a body aligned with the field, the induced body-axis voltage is

$$\Delta V_{\text{body}} \approx E L_{\text{body}} \cos\theta \tag{6}$$

where ΔV_{body} is the induced voltage along the body axis, E is the external electric field strength, L_{body} is the effective body length along the field direction, and θ is the angle between the body axis and the field direction. A larger target therefore couples a larger induced voltage at the same external field and does not necessarily require a higher applied voltage. Orientation, species, physiological condition, and swimming speed remain important. Because the electric field is established almost instantaneously at 100 Hz, target speed mainly affects the time spent within the effective field zone. Control should therefore begin from a validated field setting and adjust pulse-train duration or electrode activation according to the observed response.

The present hardware provides three open-loop control variables: output amplitude through the 2–10 V input, repetition rate through STM32 timing, and active pulse width through the PWM duty ratio. Dead time prevents simultaneous conduction of complementary switches. Isolated voltage and current sensing circuits were reserved. For larger installations, distributed electrode modules can be activated selectively, and pulse-train duration or the number of active modules can be adjusted according to the observed response, while keeping current and non-target exposure within conservative limits.

5 Conclusion

This study developed a bioelectric-barrier prototype inspired by the electric eel discharge mechanism. The design follows a two-level biomimetic logic: functionally, electric eel EOD timing defines the target waveform; structurally, cascaded Marx stages emulate the voltage-summation mechanism of serially connected electrocytes, converting low-voltage energy storage into high-voltage pulsed output. Under a 5–10 V low-voltage supply, the prototype stably generated biomimetic pulses with a repetition rate of 100 Hz and an active pulse width of 2.5 ms. The prototype achieved a voltage efficiency of 88% with a 53 V peak output. In addition, at an energy efficiency of approximately 56.5%, the main-circuit power stayed below 15 W, validating the feasibility of this topology for constructing a low-power bioelectric barrier.

Just Accepted

The underwater biological tests showed that fish produced clear behavioral responses to the generated EOD-like pulses. Compared with DC stimulation, the biomimetic EOD pulses produced stronger responses at similar peak voltages, indicating that the biomimetic pulse timing can produce stronger behavioral responses under the tested conditions. These findings suggest that a contactless, low-power underwater defense barrier based on bioelectric discharge mechanisms has engineering potential for port protection, marine ranching, and underwater infrastructure security.

Acknowledgements

None.

Author contribution statement

Chunwei Cai and Shuai Wu are responsible for Conceptualization. Chunwei Cai and Shuai Wu are responsible for Funding acquisition. Chenxu Wang, Xiao He and Shuai Wu are responsible for Methodology. Changhua Li and Xiao He are responsible for Investigation. Chenxu Wang, Xiao He and Changhua Li are responsible for Validation. All the authors are responsible for Writing – review & editing. All the authors have approved the final manuscript.

Data availability

The data that support the findings of this study are available from the corresponding author upon reasonable request.

Declaration of competing interest

All the contributing authors report no conflicts of interest in this work.

Funding

This work is granted by the Taishan Scholars of Shandong Province (Grant No. tsqnz20240801) and the National Natural Science Foundation of China (Grant No. 52401406).

Use of AI statement

During the preparation of this work, the authors used DeepSeek in order to polish the grammar, correct language errors and improve the readability of the manuscript. After using this tool, the authors reviewed and edited the content as needed and take full responsibility for the content of the publication.

Just Accepted

REFERENCES

[1] Zhang, Y. M., Wu, J., Liu, C., Tang, H. M., Mao, X. K., Yin, F. H., Tang, Y. (2025). Overview of underwater wireless power transfer based on magnetic coupling. Ocean, 1, 9470008. https://doi.org/10.26599/OCEAN.2025.9470008.

[2] Liang, Z. J., Xu, P., Fan, Y. W., Chen, D. Y., Yang, K. D. (2026). Analysis of the morphological characteristics of the Black Ghost Knifefish anal fin resulting in highly maneuverable locomotion. Ocean, 2, 9470021. https://doi.org/10.26599/OCEAN.2026.9470021.

[3] Catania, K. C. (2014). The shocking predatory strike of the electric eel. Science 346, 1231–1234. https://doi.org/10.1126/science.1260807.

[4] Catania, K. C. (2015). Electric eels concentrate their electric field to induce involuntary fatigue in struggling prey. Curr. Biol. 25, 2889–2898. https://doi.org/10.1016/j.cub.2015.09.036.

[5] Catania, K. C. (2015). Electric eels use high-voltage to track fast-moving prey. Nat. Commun. 6, 8638. https://doi.org/10.1038/ncomms9638.

[6] Catania, K. C. (2016). Leaping eels electrify threats, supporting Humboldt's account of a battle with horses. Proc. Natl. Acad. Sci. U.S.A. 113, 6979–6984. https://doi.org/10.1073/pnas.1604009113.

[7] Grundfest, H. (1957). The mechanisms of discharge of the electric organs in relation to general and comparative electrophysiology. Prog. Biophys. Biophys. Chem. 7, 1–85. https://doi.org/10.1016/S0096-4174(18)30123-9.

[8] Gallant, J. R., Traeger, L. L., Volkening, J. D., et al. (2014). Genomic basis for the convergent evolution of electric organs. Science 344, 1522–1525. https://doi.org/10.1126/science.1254432.

[9] Cao, X., Song, Z., Horng, T. L., Huang, H. (2020). Electric potential generation of electrocytes: Modelling, analysis, and computation. J. Theor. Biol. 487, 110107. https://doi.org/10.1016/j.jtbi.2019.110107.

[10] Elgenedy, M. A., Massoud, A. M., Ahmed, S., Williams, B. W., McDonald, J. R. (2019). A modular multilevel voltage-boosting Marx pulse-waveform generator for electroporation applications. IEEE Trans. Power Electron. 34, 10575–10589. https://doi.org/10.1109/TPEL.2019.2899974.

[11] Bluhm, H. (2006). Pulsed Power Systems: Principles and Applications. Springer, Berlin.

[12] Qiu, X., Su, J., Li, Y., et al. (2024). Theoretical investigation on double-matched Marx generators. IEEE Trans. Power Electron. 39. https://doi.org/10.1109/TPEL.2024.3389996.

[13] Yang, S., Yu, R., Sun, J., et al. (2024). Study on a coaxial stacked Blumlein pulse generator with inner conductors connected in parallel. IEEE Trans. Plasma Sci. 52, 5241–5248. https://doi.org/10.1109/TPS.2024.3501306.

[14] Redondo, L. M. (2010). A DC voltage-multiplier circuit working as a high-voltage pulse generator. IEEE Trans. Plasma Sci. 38, 2725–2729. https://doi.org/10.1109/TPS.2010.2050495.

[15] Zabihi, S., Zabihi, Z., Zare, F. (2011). A solid-state Marx generator with a novel configuration. IEEE Trans. Plasma Sci. 39, 1721–1728. https://doi.org/10.1109/TPS.2011.2155102.

Just Accepted

[16] Noatch, M. R., Suski, C. D. (2012). Non-physical barriers to deter fish movements. Environmental Reviews 20, 71–82. https://doi.org/10.1139/A2012-001.

[17] Parasiewicz, P., Wiśniewolski, W., Mokwa, M., Zioła, S., Prus, P., Godlewska, M. (2016). A low-voltage electric fish guidance system—NEPTUN. Fisheries Research 181, 25–33. https://doi.org/10.1016/j.fishres.2016.03.015.

[18] Tutzer, R., Röck, S., Walde, J., et al. (2021). Ethohydraulic experiments on the fish protection potential of the hybrid system FishProtector at hydropower plants. Ecological Engineering 171, 106370. https://doi.org/10.1016/j.ecoleng.2021.106370.

[19] Layhee, M. J., Sepulveda, A. J., Shaw, A., Smuckall, M., Kapperman, K., Reyes, A. (2016). Effects of electric barrier on passage and physical condition of juvenile and adult rainbow trout. Journal of Fish and Wildlife Management 7, 28–35. https://doi.org/10.3996/042015-JFWM-039.

[20] Miller, M., Sharkh, S. M., Kemp, P. S. (2024). Laying the foundations for selective-fish guidance using electricity: Multi-species response to pulsed direct currents. PeerJ 12, e17962. https://doi.org/10.7717/peerj.17962.

[21] Boute, P. G., Hagmayer, A., Smid, K., Pieters, R. P. M., Lankheet, M. J. (2024). Behavioural response thresholds of marine fish species for pulsed electric fields. Frontiers in Marine Science 10, 1286149. https://doi.org/10.3389/fmars.2023.1286149.

[22] Yi, W., Cai, L., Tan, Y., et al. (2025). Pulse frequency and water velocity determine crossing probability in pulsed direct-current fish barriers. Fishes 10, 510. https://doi.org/10.3390/fishes10100510.

[23] Yamada, Y., Kitazumi, Y., Shirai, O. (2024). Elucidation of rapid synchronization on electric discharge by use of model cell systems mimicking electric organs of electric eel. Electrochemistry 92, 022017. https://doi.org/10.5796/electrochemistry.23-68136.

[24] Xiao, X., Mei, Y., Deng, W., Zou, G., Hou, H., Ji, X. (2024). Electric eel biomimetics for energy storage and conversion. Small Methods 8, 2201435. https://doi.org/10.1002/smtd.202201435.

[25] de Santana, C. D., Crampton, W. G. R., Dillman, C. B., et al. (2019). Unexpected species diversity in electric eels with a description of the strongest living bioelectricity generator. Nature Communications 10, 4000. https://doi.org/10.1038/s41467-019-11690-z.

[26] Bray, I. E., Alshami, I. J. J., Kudoh, T. (2022). The diversity and evolution of electric organs in Neotropical knifefishes. EvoDevo 13, 9. https://doi.org/10.1186/s13227-022-00194-5.

Just Accepted